Multiple CEST contrast imaging of nose-to-brain drug delivery using iohexol liposomes at 3T MRI

Lok Hin Law [a,1], Jianpan Huang [a,1], Peng Xiao [a], Yang Liu [a], Zilin Chen [a], Joseph H.C. Lai [a], Xiongqi Han [a], Gerald W.Y. Cheng [b], Kai-Hei Tse [b], Kannie W.Y. Chan [a,c,d,e,f,*]

[a] Department of Biomedical Engineering, City University of Hong Kong, Hong Kong, China
[b] Department of Health Technology and Informatics, The Hong Kong Polytechnic University, Hong Kong, China
[c] Russell H. Morgan Department of Radiology and Radiological Science, Johns Hopkins University School of Medicine, Baltimore, MD, United States
[d] City University of Hong Kong Shenzhen Research Institute, Shenzhen, China
[e] Tung Biomedical Science Centre, City University of Hong Kong, Hong Kong, China
[f] Hong Kong Centre for Cerebro-cardiovascular Health Engineering, Hong Kong, China

ARTICLE INFO

ABSTRACT

Image guided nose-to-brain drug delivery provides a non-invasive way to monitor drug delivered to the brain, and the intranasal administration could increase effective dose via bypassing Blood Brain Barrier (BBB). Here, we investigated the imaging of liposome-based drug delivery to the brain via intranasal administration, in which the liposome could penetrate mucus and could be detected by chemical exchange saturation transfer (CEST) magnetic resonance imaging (MRI) at 3T field strength. Liposomes were loaded with a computed tomography (CT) contrast agent, iohexol (Ioh-Lipo), which has specific amide protons exchanging at 4.3 ppm of Z-spectrum (or CEST spectrum). Ioh-Lipo generated CEST contrasts of 35.4% at 4.3 ppm, 1.8% at −3.4 ppm and 20.6% at 1.2 ppm in vitro. After intranasal administration, these specific CEST contrasts were observed in both olfactory bulb (OB) and frontal lobe (FL) in the case of 10% polyethylene glycol (PEG) Ioh-Lipo. We observed obvious increases in CEST contrast in OB half an hour after the injection of 10% PEG Ioh-Lipo, with a percentage increase of 62.0% at 4.3 ppm, 10.9% at −3.4 ppm and 25.7% at 1.2 ppm. Interestingly, the CEST map at 4.3 ppm was distinctive from that at −3.4 pm and 1.2 ppm. The highest contrast of 4.3 ppm was at the external plexiform layer (EPL) and the region between left and right OB (LROB), while the CEST contrast at −3.4 ppm had no significant difference among all investigated regions with slightly higher signal in olfactory limbus (OL, between OB and FL) and FL, as validated with histology. While no substantial increase of CEST contrast at 4.3 ppm, −3.4 ppm or 1.2 ppm was observed in OB and FL when 1% PEG Ioh-Lipo was administered. We demonstrated for the first time the feasibility of non-invasively detecting the nose-to-brain delivery of liposomes using CEST MRI. This multiple-contrast approach is necessary to image the specific distribution of iohexol and liposome simultaneously and independently, especially when designing drug carriers for nose-to-brain drug delivery.

1. Introduction

Drug delivery to the central nervous system (CNS) is challenging due to the presence of blood-brain-barrier (BBB), since most therapeutic molecules cannot pass through the BBB from the bloodstream [1–4]. Thus, oral and intravenous administrations are ineffective [2,5]. Intranasal drug delivery provides an alternative route to enhance the efficiency of drug delivery to the brain via bypassing the BBB. Many studies have reported increased effective dose to the brain by intranasal administration compared to oral administration or intravenous injection [5–7]. Direct intracerebral or intrathecal administration could increase the effective dose, however, it can be highly invasive and lead to other complications [8–10]. Moreover, intranasal delivery is also a common administration route for vaccination [11]. The only barrier in the intranasal cavity is the mucus. One way to facilitate mucus penetration is to incorporate sufficient percentage of polyethylene glycol (PEG) onto liposomes. Nanoparticles with dense coating of PEG can effectively avoid mucoadhesion and achieve rapid mucus penetration [12–14].

Hanes et al. have shown that increasing PEG content of polymeric particles could lead to the formation of hydrophilic and nearly neutrally charged polymeric particles, which can effectively avoid mucoadhesion by reducing hydrophobic or electrostatic interactions [15,16]. These mucus penetrating particles achieved rapid mucus penetration [13,14,17,18]. They have also shown that increasing PEG content in polymeric particles is one of the strategies to achieve mucus penetration in lung or airway [19,20]. Liposome is a versatile drug carrier that has an aqueous core and lipid bilayer for both hydrophilic and hydrophobic drugs respectively. It enables a relatively high local concentration and a sustainable release of drugs [21]. Furthermore, lipid-based nanoparticles could enhance brain targeting [22,23]. Our previous studies demonstrated that ≥7 mol%-PEG liposomes provide improved mucus penetrating ability and distribution compared to 0 and 3 mol%-PEG liposomes, measured by Chemical Exchange Saturation Transfer (CEST) contrast generated by intraliposomal barbituric acid (BA) [12,24]. Liposomes with ~7 mol%-PEG were coated with brush-like PEG chains, forming effective surface shielding and achieving the best mucus penetrating ability among 0–12 mol%-PEG liposome formulations [12].

Non-invasive methods for imaging the drug delivery and biodistribution in the brain could provide valuable information for treatment refinements, such as liposomes [25,26]. In particular, it enables the assessment of delivery pathway and amount of drug delivered to specific brain regions, which could inform the design of delivery vehicles to improve delivery and bioavailability. CEST is a molecular contrast mechanism in magnetic resonance imaging (MRI), which enables sensitive and non-invasive detection of molecules via their exchangeable protons [27,28]. CEST MRI has been applied for imaging endogenous proteins [29–31] and a variety of molecules, such as glucose [32–34], creatine [35,36] and glutamate [36,37]. One advantage of CEST is to detect molecules in their natural forms in vivo without additional metallic or radioactive labels [27,28], for example, the amide protons of proteins [29–31] and the hydroxyl protons of glucose [32–34,38,39]. Due to its non-invasive nature, CEST MRI has become a common examination for assessing brain tumors at multiple sites [40–42]. In addition to the endogenous CEST contrasts, many molecules or agents that are approved for clinical use contain CEST detectable protons. For example, computed tomography (CT) contrast agents have been reported to serve as CEST contrast agents in the presence of amide protons, in particular, they were applied to facilitate pH imaging in cancers [43–45]. Many studies also reported that CT agents have strong CEST contrasts at multiple offsets of the *Z*-spectrum (CEST spectrum acquired for characterization of contrast) [43,46–48]. Chen et al. have developed a CT and CEST MRI bimodal imaging to monitor iodinated liposomes and found that iodixanol-loaded liposomes exhibited strong CEST contrasts at 4.3 ppm (amide protons) and 1.0 ppm (hydroxyl protons) with similar contrast and magnitude to their non-liposomal form [49]. Moreover, the water accessibility and size of liposomes can be tailored to further enhance the CEST contrast and facilitate the imaging of multiple CEST contrast [21,50]. The ability to detect multiple exchangeable protons at the same time is another advantage of CEST MRI [50–52].

In our previous study, we have demonstrated that this multiple contrast is a robust approach to monitor different release rates of drug and liposome, simultaneously and independently [51]. The CEST contrast at −3.4 ppm attributed to the phospholipid bilayers of liposomes could be used to monitor the amount of liposomes delivered [21,51]. Conventionally, relayed nuclear Overhauser effect (rNOE) refers to the CEST contrast from 0 ppm to −5 ppm, which is related to the aliphatic protons and their relayed exchange with water [27]. In the brain, rNOE provides valuable information about changes in mobile proteins/lipids and potentially bound molecules in vivo [53–58], for example, imaging brain tumor [58], stroke [55] and demyelination in multiple sclerosis [56,57].

Herein, we developed a CEST detectable liposome that can penetrate mucus for imaging and tracking the intranasal drug delivery from nose to brain at 3T MRI (Fig. 1). Multiple CEST contrasts of iohexol loaded liposome (Ioh-Lipo) at 4.3 ppm, 1.2 ppm and −3.4 ppm could be applied to monitor iohexol and liposome independently in both phantom and in vivo. We also studied the biodistribution of iohexol and liposome in specific regions in olfactory bulb (OB) and frontal lobe (FL) after intranasal administration, which was validated by histology. Our study demonstrated the potential of image-guided nose-to-brain liposomal drug delivery using molecular CEST MRI.

2. Materials and methods

CT Contrast agents (iohexol) were purchased from GE Healthcare Life Sciences (Pittsburg, PA). 1,2-distearoyl-sn-glycero-3-phosphocholine (DSPC), 1,2-distearoyl-sn-glycero-phosphoethanolamine poly (ethylene glycol) 2000 (DSPE-PEG-2000), 1,2-dioleoyl-sn-glycero-3-phosphoethanolamine-N (lissamine rhodamine B sulfonyl) and cholesterol were purchased from Avanti Polar Lipids, Inc. (Alabaster, AL). Sephadex G50 columns were bought from GE Healthcare Life Sciences (Pittsburg, PA). RPMI 2650 cell line was purchased from ATCC (Manassas, VA). Eagle's Minimum Essential Medium (EMEM), phosphate-buffered saline (PBS, pH 7.4), fetal bovine serum (FBS), penicillin-streptomycin and trypsin were all purchased from Gibco, Invitrogen. 4′,6-diamidino-2-phenylindole (DAPI) was purchased from Thermo Fisher Science (Waltham, MA). All the chemicals and solvents used in the study were of analytical grade and purchased from Sigma-Aldrich (St. Louis, MO, USA). Deionized water was used throughout the experiments.

2.1. CT agent solution preparation

In our study, CT agent iohexol (MW = 821.138 g/mol) was prepared for the in-vitro experiment. 700 μl iohexol solution with concentration of 647 mg/ml (787.9 mM) was dissolved in 500 μl distilled water in 7.0 pH to prepare a 459.6 mM iohexol solution.

2.2. Iohexol-loaded liposome preparation

Iohexol encapsulated liposome (Ioh-Lipo) was prepared through thin film hydration [21], and extrusion method using a formulation of DSPC: cholesterol:DSPE-PEG2000:rhodamine = 50:40:10:0.18 for 10% PEG Ioh-Lipo, and 55:44:1:0.18 for 1% PEG Ioh-Lipo. This formulation was designed with reference to the clinical formulation of Doxil [59], in which DSPC and cholesterol formed a stable phospholipid bilayer [60–62]; DSPE-PEG2000 was coated on the surface of liposomes to enhance the mucus penetration; and rhodamine B was added to enable the histological analysis of the liposome distribution in the brain. Lipid mixture was dissolved in chloroform and evaporated to form a dry homogeneous thin film layer by a rotary evaporator (Heidolph, Schwabach, Germany). The lipid film was then rehydrated with the CT contrast agents (700 μl of iohexol with 500 μl distilled water) with temperature higher than the transition temperature of the lipid, and sonicated for 30 min to form large multilamellar liposomes (MLVs). The solution was finally extruded through 400 nm polycarbonate membranes for 15 times then through 200 nm polycarbonate membranes for another 15 times to obtain the resultant liposome with size <150 nm. For 10% PEG Ioh-Lipo with size > 200 nm, liposome solution only passed through the 400 nm membrane. The unloaded agent of the resultant liposome solution was filtered through Sephadex G-50 gel columns twice before imaging.

2.3. Liposome characterization

The size, polydispersity index (PDI) and surface charge of liposomes were measured by dynamic light scattering (DLS) at room temperature by Zetasizer (Malvern Instruments, UK). The particle concentration was measured by Nanosight (Malvern Instruments, UK).
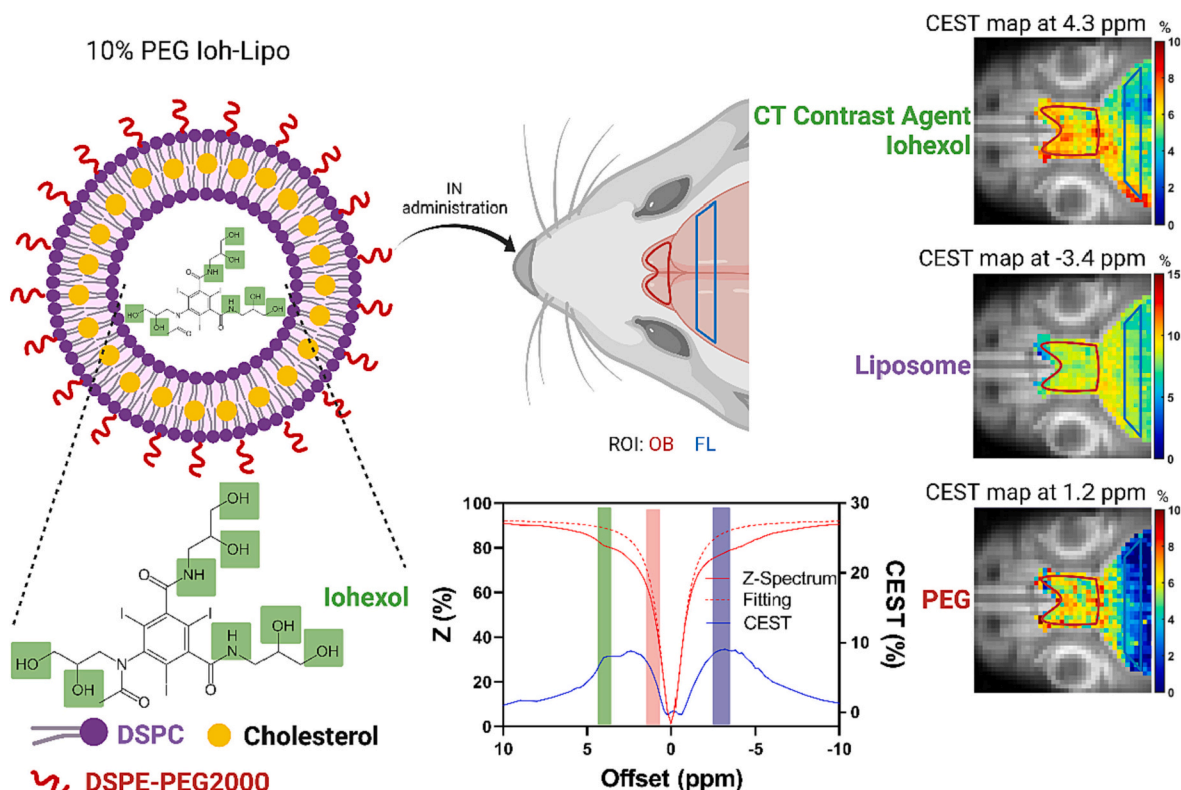
Fig. 1. Schematic illustration for the development of multiple CEST contrast imaging of nose-to-brain drug delivery. Structure of CT contrast agent (iohexol) loaded mucus penetrating liposomes (10% PEG Ioh-Lipo), which have CEST detectable exchangeable protons, including -NH and -OH of iohexol (in green), phospholipid bilayer (in purple) and -OH on PEG (in red). Their corresponding distributions in the brain are represented by CEST maps at 4.3 ppm, −3.4 ppm and 1.2 ppm, respectively. Created with BioRender.com (For interpretation of the references to colour in this figure legend, the reader is referred to the web version of this article.)

2.4. Iohexol release study

The loading of iohexol in liposomes was estimated by measuring the UV absorbance at 245 nm using UV-VIS spectrometer (PerkinElmer, MA, USA). Ioh-Lipo was treated with Triton X-100 solution to completely release the iohexol payload, diluted to proper concentration, followed by UV measurements. The concentration was then determined by the calibration curve of iohexol solutions with known concentrations.

Iohexol release from liposomes was studied using a dialysis method. Dialysis bags were soaked before use in distilled water at room temperature for 12 h to remove the preservative, followed by rinsing thoroughly in distilled water. The release experiments were done immediately after the preparation of liposomes. The liposome stock solution was diluted 10 times. The resulting liposome solution of 500 μl was transferred in dialysis bag (cut off molecular weight: 3000/5000) and immersed into 10 mL PBS solution. The sac was placed inside a conical flask with the help of a glass rod so that the portion of the dialysis sac with the formulation dipped into the buffer solution. The flask was kept on a magnetic stirrer and stirring was maintained at 100 rpm at 37 °C with a thermostatic control. 2 mL supernatant was taken out and re-supplemented with fresh PBS at 0.25, 0.5, 1, 2, 4, 6, 9, 24 and 48 h, respectively, followed by UV measurements at 245 nm [51].

2.5. ^{1}H NMR experiment

A weighted sample of dried 10% PEG Ioh-Lipo or 1% PEG Ioh-Lipo (30 mg) was dissolved in D$_2$O. An aliquot of sample (500 μL) was placed into a 5-mm NMR tube [52,63]. NMR spectra (0–10 ppm) were acquired by Bruker 400 MHz "AVANCE III"Nuclear Magnetic Resonance System (NMR-400) (Bruker, Ettlingen, Germany). Chemical shifts of iohexol were at 3.89 ppm (C-OH), and PEG backbone at 3.54 ppm (other assignments were shown in Supplementary Fig. 1) [64,65]. Integrals at

3.54 ppm were used to calculate the PEG content.

2.6. Cell preparation and mucus retention study

Human nasal epithelial cell RPMI 2650 was used for liposome retention cell study. The cells were seeded in 12-wells-plate and maintained in DMEM supplemented with 10% FBS and 1% Penicillin-Streptomycin. The cell cultures were maintained at 37 °C in a > 95% humidified atmosphere of 5% CO$_2$ in air with media changes on alternate days. The cell was in culture for 14 days, and after 100% confluence for mucus secretion. Mucus was confirmed by Alcian blue staining (Supplementary Fig. 2). Alcian blue staining was performed on day 1, 7, and 14 after cells were at confluence. 10% PEG Ioh-Lipo and 1% PEG Ioh-Lipo were diluted with the cell culture medium and added in each well for 0.5, 1 and 2 h [12,66,67]. The liposome mixture in the culture plate was removed and cells were gently washed by PBS three times, to ensure liposomes were penetrated the mucus rather than on the surface of mucus [68]. Then, the rhodamine signal of liposomes in the wells was measured by microplate reader at 560/580 nm of excitation/emission wavelength (Molecular Devices, CA, USA). A calibration curve was obtained for fluorescence signal and corresponding liposome concentration (Supplementary Fig. 3). Three independent experiments were performed to ensure reproducibility of this mucus retention study.

2.7. In vitro CEST MRI measurement

In-vitro MRI images for phantom experiments of drug solutions and drug encapsulated liposome were acquired on a horizontal bore 3T Bruker BioSpec system (Bruker, Ettlingen, Germany) equipped with a 40-mm volume transceiver coil. The CEST sequence was rapid acquisition with relaxation enhancement (RARE) sequence with a continuous wave (CW) pre-saturation module. The parameters were set as

following: slice thickness = 2 mm, field of view (FOV) = 26 × 24 / 30 × 9 mm^2 for the iohexol solution/Ioh-Lipo phantom, image size = 32 × 32, RARE factor = 32, repetition time/echo time (TR/TE) = 6000/77 ms. Saturation power (B_1) was varied as: 0.6, 0.8, 0.9, 1.0, 1.2, 1.4 μT, with a saturation time (t_{sat}) of 3 s. CEST frequency was varied from −15 to +15 ppm, with a step size of 0.2 ppm between −6 to 6 ppm, a step size of 1 ppm between ±6 and ±15 ppm and additional acquisition points at ±2.1, ±2.25, ±2.3, ±2.35, ±2.45, ±2.5, ±4.1, ±4.25, ±4.3, ±4.35, ±4.5 ppm and ±20 ppm. Three M_0 images at 200 ppm were acquired for normalization. Thus, the total scan time of a CEST acquisition was 10 min 36 s.

2.8. Animal preparation

The Animal Research Ethics Sub-Committee and the Institutional Laboratory Animal Research Unit of City University of Hong Kong approved all animal experiments and animal registration in this study. All animals were housed under standard laboratory conditions, with access to food and water. Six 12 weeks-old male ICR mice were used for intranasal administration [69] of CT agents loaded liposome. 150 μl of liposomal solution was administrated intranasally to one side of the nasal cavity by pipette into the ICR mouse.

2.9. In vivo MRI

T2-weighted (T2w) and CEST images were acquired pre-injection and 0.5, 1 and 1.5 h after intranasal injection of Ioh-Lipo. Treated mouse remained under anesthesia for 30 min before imaging, to ensure sufficient time for the transportation and penetration of liposomes into the mucus [67]. The in-vivo MRI images for intranasal administration experiments at the olfactory bulb of mice were acquired on a horizontal bore 3T Bruker BioSpec system (Bruker, Ettlingen, Germany) equipped with one 82 mm quadrature volume resonator as a transmitter and a single surface coil as a receiver. The T2 weighted image and CEST data in axial view were acquired. The CEST sequence was RARE sequence with a CW pre-saturation module. The parameters were set as following: slice thickness = 2 mm, FOV =16 × 16 mm^2, image size = 64 × 64, RARE factor = 32, TR/TE = 5000/5 ms. B_1 was varied as: 0.6, 0.9 μT, with t_{sat} of 3 s. CEST frequency was varied from −15 to +15 ppm, with a step of 0.2 ppm between −6 to 6 ppm, a step of 1 ppm between ±6 and ±15 ppm and extra acquisition points on ±2.1, ±2.25, ±2.3, ±2.35, ±2.45, ±2.5, ±4.1, ±4.25, ±4.3, ±4.35, ±4.5 ppm and ±20 ppm. Three M_0 images at 200 ppm were acquired for normalization. Thus, the total scan time of a CEST acquisition was 14 min 10 s.

2.10. Data analysis

The CEST data were processed by custom-written MatLab (Mathworks, Natick, MA) code. After acquiring CEST data, the raw Z-spectra (Z) were formed by [27,70]:

$$Z(\Delta\omega) = \frac{S_{sat}(\Delta\omega)}{S_0} \tag{1}$$

where $\Delta\omega$ presented the frequency offsets, while $S_{sat}(\Delta\omega)$ and S_0 were the magnetization signals with saturation and without saturation, respectively. After the raw Z-spectra formation, the B_0 correction was performed on a pixel-wise basis. Lorentzian difference analysis [71] was adopted for calculating CEST contrasts. The Lorentzian line shape function could be expressed as [71,72]:

$$L_i(\Delta\omega) = \frac{A_i}{1 + \left[\frac{\Delta\omega - \delta_i}{\Gamma_i/2}\right]^2} \tag{2}$$

where A_i represented the peak amplitude, Γ_i represented the full-width-at-half-maximum (FWHM) and δ_i represented the peak position. The δ_i

was set to 0 ppm for direct water saturation (DS) and −2.5 ppm for magnetization transfer (MT) as the B_0 was corrected. The Z-spectrum data from −0.8 ppm to 0.8 ppm, and from ±10 ppm to ±20 ppm were used for the fitting of reference curve (Z_{ref}). For the in vitro phantom data, DS effect was fitted to obtain Z_{ref} [71]:

$$Z_{ref}(\Delta\omega) = 1 - L_{DS}(\Delta\omega) \tag{3}$$

For the in vivo data, both DS and MT effects were fitted to obtain Z_{ref} [73,74]:

$$Z_{ref}(\Delta\omega) = 1 - L_{DS}(\Delta\omega) - L_{MT}(\Delta\omega) \tag{4}$$

The CEST contrast (%) was quantified by subtracting the Z-spectrum from the fitted reference curve:

$$CEST(\Delta\omega) = \left[Z_{ref}(\Delta\omega) - Z(\Delta\omega) \right] \times 100\% \tag{5}$$

2.11. Histology

After MRI, three mice per group were sacrificed with 2% isoflurane gas and then intracardially perfused with PBS. Whole brains were harvested and fixed in formalin and dehydrated in sucrose before cryosectioning. Axial slices at 20-μm thickness were sectioned and mounted, and three slices per animal were included for further analysis. Liposomal distribution in the brain sections were detected by the rhodamine-labeled liposomes, and the nuclei were stained by DAPI. The Axial brain sections were imaged with Leica TCS SP8 confocal microscopy system (Leica Microsystem, Germany).

3. Results

3.1. CEST characterization of CT contrast agents

CEST properties of iohexol solution was firstly examined in vitro and results were shown in Fig. 2. The iohexol ($n = 3$) at 459.6 mM and 7.0 pH showed strong CEST contrast at 4.3 ppm for all investigated B_1 powers (Fig. 2a&b). The CEST contrast increased from 35.2 ± 0.1% to 61.7 ± 0.1% when the B_1 power increased from 0.6 μT to 1.4 μT (Fig. 2c). This indicated that iohexol can be sensitively detected by CEST MRI even at a low power (0.6 μT) at low field strength (3T). The CEST contrast increased linearly from 8.5 ± 0.2% to 33.7 ± 0.1% ($R^2 = 0.9974$) when the concentration of iohexol solution increased from 98.4 mM to 459.6 mM, as shown in Fig. 2d.

3.2. Characterization of iohexol loaded liposomes (Ioh-Lipo)

With reference to our previous studies [12], we studied two liposome formulations, i.e. Ioh-Lipo with 10% PEG and 1% PEG. We characterized the properties of liposomes, including particle size, PDI, zeta potential and particle concentration (Table 1). The 10% PEG Ioh-Lipo ($n = 3$) had a particle size of 166.3 ± 1.5 nm, PDI of 0.2 ± 0.02 and zeta potential of −6.8 ± 0.07 mV. At a comparable particle concentration, the 1% PEG Ioh-Lipo (n = 3) had a particle size of 173.9 ± 0.4 nm, PDI of 0.2 ± 0.01 and zeta potential of −4.4 ± 0.04 mV. We also confirmed the PEG content is >10 times higher in 10% PEG Ioh-Lipo than in 1% PEG Ioh-Lipo by NMR (Supplementary Fig. 1), where peak at 3.54 ppm indicated the PEG and peaks at 3.2–4.0 ppm indicated the iohexol.

3.3. Release and in vitro mucus retention study

The release profiles for both 10% PEG Ioh-Lipo and 1% PEG Ioh-Lipo were monitored for 3 days (Fig. 3a). The zoom-in release profiles within 6 h were shown in Supplementary Fig. 4. 10% PEG Ioh-Lipo released 36.5% after an hour and reached a plateau at around 9 h. The maximum accumulative release was up to 67.7% after 48 h. While 1% PEG Ioh-Lipo released 35.7% after an hour and reached the plateau at around 9 h. The maximum accumulative release is up to 66.0% after 48 h.
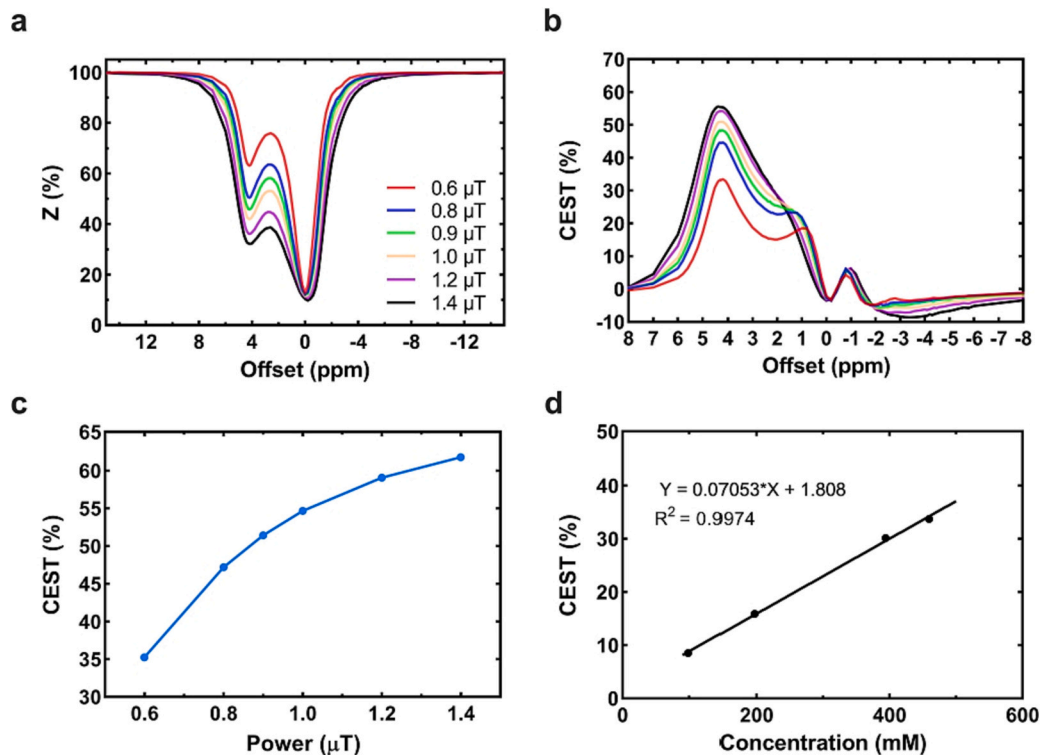
Fig. 2. CEST properties of iohexol solution ($n = 3$). (a) Z-spectra and (b) CEST spectra of Ioh-Lipo under pH = 7.0, acquired by using different B_1 powers. (c) B_1 power dependency and (d) concentration dependency of iohexol solution.

Table 1
Characterization of Ioh-Lipo with different PEG concentration ($n = 3$).

Liposome	Concentration (particles/ml)	Size (nm)	PDI	Zeta Potential (mV)
10% PEG Ioh-Lipo	3.67×10^{16}	166.3 ± 0.7	0.2 ± 0.02	-6.8 ± 0.07
1% PEG Ioh-Lipo	5.90×10^{16}	173.9 ± 0.4	0.2 ± 0.01	-4.4 ± 0.40

We performed the mucus retention study using RPMI 2650 cells. We added rhodamine-labeled liposomes with either 10% PEG or 1% PEG Ioh-Lipo onto the cells that have been cultured for 14 days, which was reported to have sufficient mucus [75–77], and confirmed with Alcian blue staining. After 30 min, 1 and 2 h of incubation, fluorescence signal was recorded to examine the mucus retention differences between 10% PEG and 1% PEG Ioh-Lipo in the mucus of the cell. We observed a 28.1% higher retention in the mucus of RPMI 2650 cells with 10% PEG Ioh-Lipo than with 1% PEG Ioh-Lipo for 0.5 h, which was 22.1% higher at 1.0 h

after incubation ($P < 0.01$). This corresponds to $4.1 \pm 0.3 \times 10^{13}$ liposomes and $8.2 \pm 1.4 \times 10^{13}$ liposomes retained after 0.5 h and 1 h, respectively (Supplementary Fig. 3). After 2 h of incubation, a total of $10.3 \pm 1.2 \times 10^{13}$ 10% PEG Ioh-Lipo retained, which corresponds to a 25.4% higher than that of 1% PEG Ioh-Lipo (Fig. 3b).

3.4. CEST characterization of iohexol loaded liposomes

CEST properties of Ioh-Lipo were examined in vitro. As shown in Fig. 4, both formulations of Ioh-Lipo ($n = 3$) showed high CEST contrast at 4.3 ppm (Fig. 4b), $35.4 \pm 0.18\%$ for 10% PEG Ioh-Lipo and $36.2 \pm 1.06\%$ for 1% PEG Ioh-Lipo; and comparable CEST contrast at -3.4 ppm (Fig. 4c), $1.8 \pm 0.07\%$ for 10% PEG Ioh-Lipo and $1.9 \pm 0.16\%$ for 1% PEG Ioh-Lipo at a B_1 power of 0.6 µT; CEST contrast at 1.2 ppm was $20.6 \pm 0.4\%$ for 10% PEG Ioh-Lipo and $16.9 \pm 0.6\%$ % for 1% PEG Ioh-Lipo. CEST contrast was acquired at a series of B_1 from 0.6 µT to 1.4 µT for optimization. At both 4.3 ppm and 1.2 ppm, CEST contrast increases as the B_1 power increased (Fig. 4d, e), which were relatively linear at 0.6–0.9 µT. The CEST contrast at -3.4 ppm of both 10% PEG Ioh-Lipo
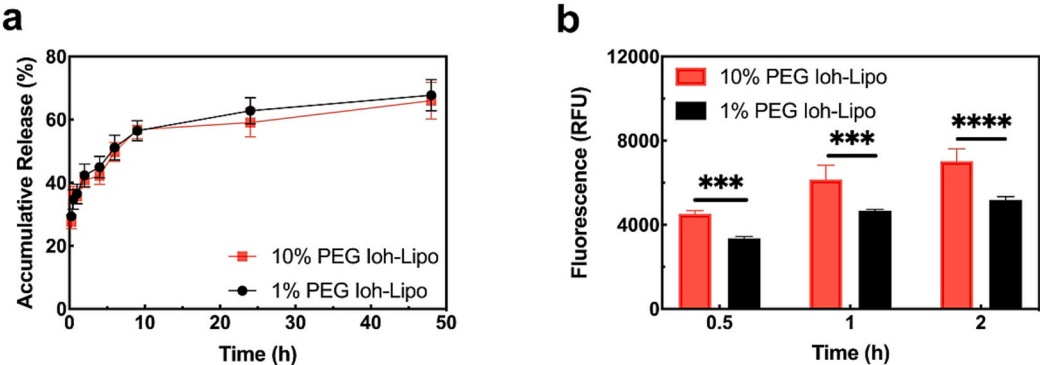

Fig. 3. Release profiles and liposome retention properties of Ioh-Lipo with different PEG concentrations. (a) Release profiles of 10% PEG and 1% PEG Ioh-Lipo ($n = 4$), and (b) In vitro mucus retention of 10% PEG and 1% PEG Ioh-Lipo with small size (<200 nm) measured at 0.5, 1 and 2 h after incubation (n = 3). Comparisons were performed using two-way ANOVA multiple comparison. Differences were considered as statistically significant for P value < 0.05 (*), P < 0.01 (**),P < 0.001 (***), and P < 0.0001 (****).
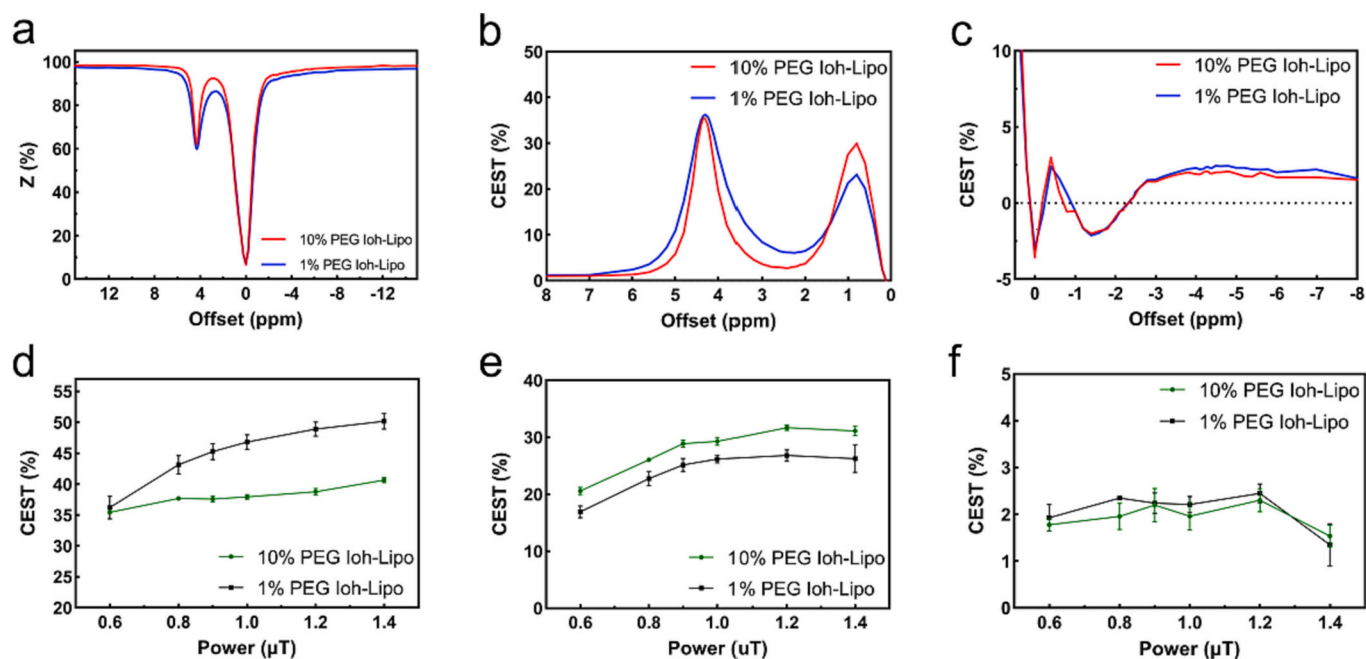
Fig. 4. CEST properties of 10% PEG and 1% PEG Ioh-Lipo ($n = 3$). (a) Z-spectra and CEST spectra of Ioh-Lipo at (b) positive and (c) negative side, under $B_1 = 0.6$ μT and pH = 7.0. B_1 power dependency of Ioh-Lipo CEST contrast at (d) 4.3 ppm, (e) 1.2 ppm and (f) −3.4 ppm.

and 1% PEG Ioh-Lipo were at around 2% when the B_1 power increased from 0.6 μT to 1.2 μT, and was much lower at 1.4 μT (Fig. 4f).

3.5. In vivo CEST MRI

Mice received 150 μl of either 10% PEG Ioh-Lipo ($n = 6$) or 1% PEG Ioh-Lipo ($n = 6$) intranasally were imaged. T2-weighted (T2w) and CEST images were acquired pre-injection and 0.5, 1, 1.5 h after injection. In the considerations of other contributions to the z-spectrum in vivo, among the optimized B_1 in vitro (Fig. 4 d-f, 0.6–0.9 μT), we compared the CEST contrast in OB at B_1 of 0.6 μT and 0.9 μT. As shown in Supplementary Fig. 5, a low saturation power could avoid large contaminations from DS and MT. Thus, Z-spectra were acquired using a B_1 power of 0.6 μT in vivo, which provides comparable CEST contrasts for 10% PEG and 1% PEG Ioh-Lipo in vitro (Fig. 4). CEST contrasts at 4.3 ppm, −3.4 ppm and 1.2 ppm were obtained from OB and FL (Figs. 5, 6, Supplementary Fig. 6, 7). In the cohort received 10% PEG Ioh-Lipo, CEST contrast increased by 62.0 ± 22.0% at 4.3 ppm and 10.9 ± 1.4% at −3.4 ppm in OB at 0.5 h after injection compared to pre-injection. Meanwhile, CEST contrast increased by 39.5 ± 12.4% at 4.3 ppm and 9.2 ± 4.3% at −3.4 ppm in FL. Interestingly, we also observed a CEST contrast enhancement at around 1.2 ppm (increased by 25.7 ± 17.8% in OB and 56.5 ± 18.2% in FL, 0.5 h after injection), which could be contributed by the hydroxyl protons of iohexol and the higher PEG content of the 10% PEG Ioh-Lipo formulation (Fig. 2b, 4b).

In contrast, mice received 1% PEG Ioh-Lipo did not show significant changes at 4.3 ppm, −3.4 and 1.2 ppm over the period of imaging (Fig. 5, 6). Distinctive peak at 4.3 ppm was consistently observed in 10% PEG Ioh-Lipo spectra (Fig. 5c, d, Supplementary Fig. 6) but not in 1% PEG Ioh-Lipo spectra (Fig. 5e, f, Supplementary Fig. 7). Moreover, we also compare with an additional control group (Supplementary Fig. 8), of which mice received 10% PEG Ioh-Lipo with size >200 nm (Supplementary Table 1). Mice received 10% PEG Ioh-Lipo with size >200 nm also did not show significant changes at 4.3, −3.4 and 1.2 ppm after injection. This is because both 1% PEG Ioh-Lipo and 10% PEG Ioh-Lipo with size >200 nm cannot pass through the mucus and reach the brain.

Notably, we observed different regional changes of CEST contrasts at 4.3 ppm, −3.4 ppm and 1.2 ppm in OB and FL among these CEST maps

of 10% PEG Ioh-Lipo (Fig. 5a). Both CEST contrasts at 4.3 ppm and −3.4 ppm of 10% PEG Ioh-Lipo were significantly higher than that of 1% PEG Ioh-Lipo (Fig. 6a-d, $P < 0.001$; P < 0.001; P < 0.05; P < 0.01, respectively) at 0.5 h after injection. CEST contrast differences were 2.2% at 4.3 ppm and 0.7% at −3.4 ppm in the OB, while 1.4% at 4.3 ppm and 0.8% at −3.4 ppm in the FL. For 10% PEG Ioh-Lipo, OB and FL increased by a similar percentage (10.9 ± 1.4% vs. 9.2 ± 4.3%) at −3.4 ppm, while OB increased more than FL at 4.3 ppm (62.0 ± 22.0% vs. 39.5 ± 12.4%).

Based on these observations, we further analyzed the CEST signal changes in small regions, such as external plexiform layer (EPL), middle region between left and right OB (LROB), granule cell layer (GCL) and olfactory limbus (OL) between OB and FL (Fig. 7a) in 10% PEG Ioh-Lipo cohort for analyzing the distribution of iohexol and liposome in the brain. We compared CEST contrast at 4.3 ppm, −3.4 ppm and 1.2 ppm at 0.5 h after injection (Fig. 7b-d). With the consideration of spatial resolution limitation, EPL and LROB were combined (EPL + LROB). At 4.3 ppm, the CEST contrast of EPL + LROB and OL were significantly higher than that of GCL and FL ($P < 0.05$). OL (4.5 ± 1.1% vs. 2.4 ± 1.8%, $P = 0.022$) and EPL + LROB (4.5 ± 1.5% vs. 2.4 ± 1.8%, $P = 0.0018$), were significantly higher than that of FL, which was slightly lower than that of GCL (3.3 ± 1.7% vs. 2.4 ± 1.8%). Among all investigated ROIs, EPL + LROB showed the highest CEST contrast which was significantly higher than that of GCL (4.5 ± 1.5% vs. 3.3 ± 1.7%, $P = 0.0013$). EPL + LROB also had the highest contrast at both 4.3 ppm and 1.2 ppm, although no significant difference at −3.4 ppm and 1.2 ppm among all ROIs (Fig. 7c, d). According to the nose-to-brain delivery pathway, liposomes could be indirectly transported to the brain by crossing the BBB after absorbed systemically, or directly transported to the brain via olfactory or trigeminal nerve pathway. These pathways will pass through the EPL layer of OB, and CSF regions which located around LROB [78]. Thus, imaging the liposome distribution in the brain could provide valuable information related to the pathways and to guide the design of drug delivery vehicle.

The distribution of liposomes was validated by histology via the rhodamine labels on liposomes. In Fig. 8, rhodamine (red) indicated the distribution of rhodamine-labeled liposomes and DAPI (blue) was the counter stain for nuclei. The DAPI signal was comparable for mice
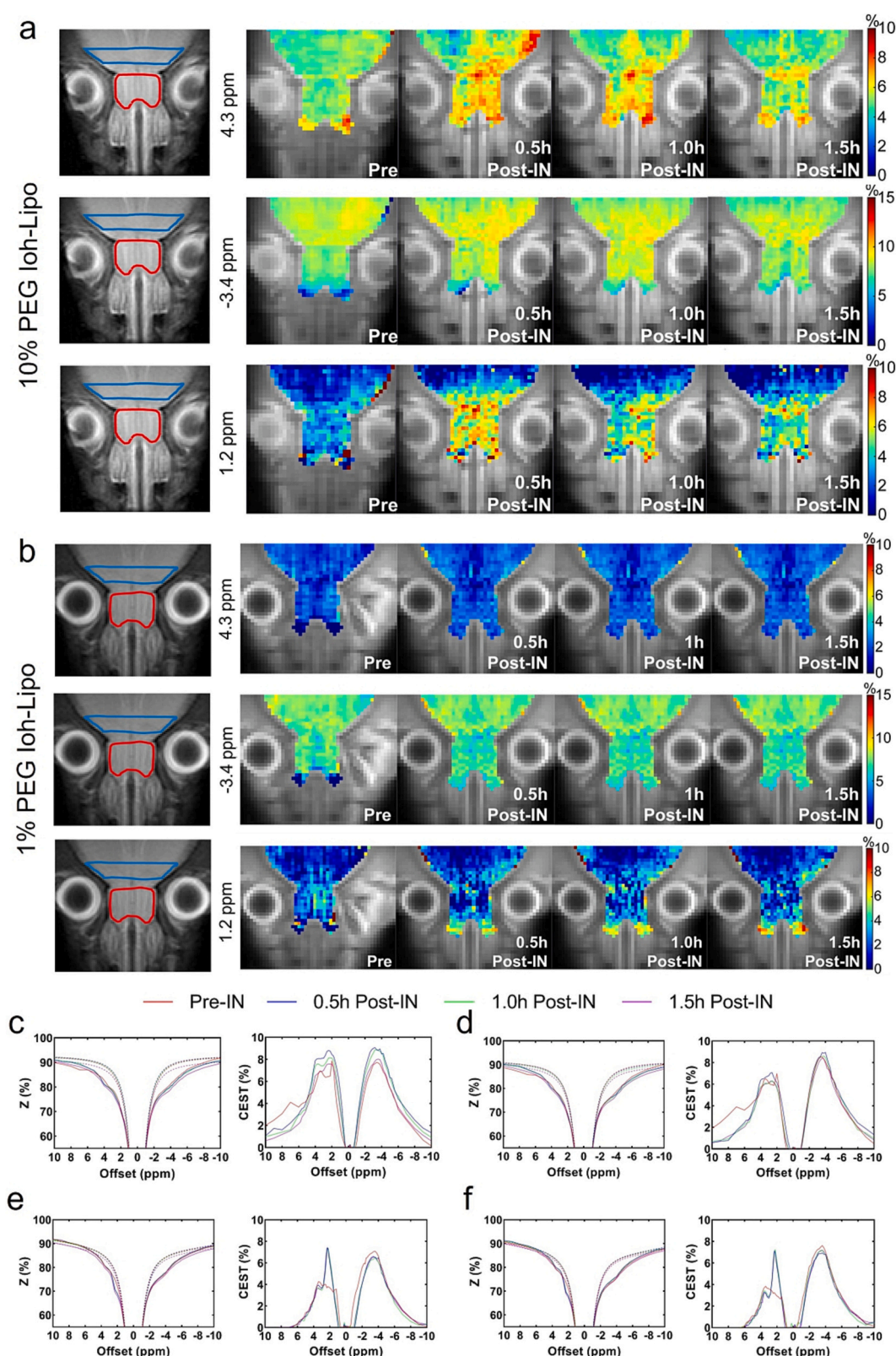
Fig. 5. In vivo experiment of intranasal administration of Ioh-Lipo in mice ($n = 6$). T2w image and CEST maps (4.3 ppm, −3.4 ppm and 1.2 ppm) at pre-injection, and 0.5, 1, 1.5 h after injection, for (a) 10% PEG Ioh-Lipo and (b) 1% PEG Ioh-Lipo. Z-spectra and CEST spectra for 10% PEG Ioh-Lipo of (c) OB and (d) FL. Z-spectra and CEST spectra for 1% PEG Ioh-Lipo of (e) OB and (f) FL. (Red and blue area in T2w images indicated the ROI for generating the Z-spectra of OB and FL, respectively). (For interpretation of the references to colour in this figure legend, the reader is referred to the web version of this article.)
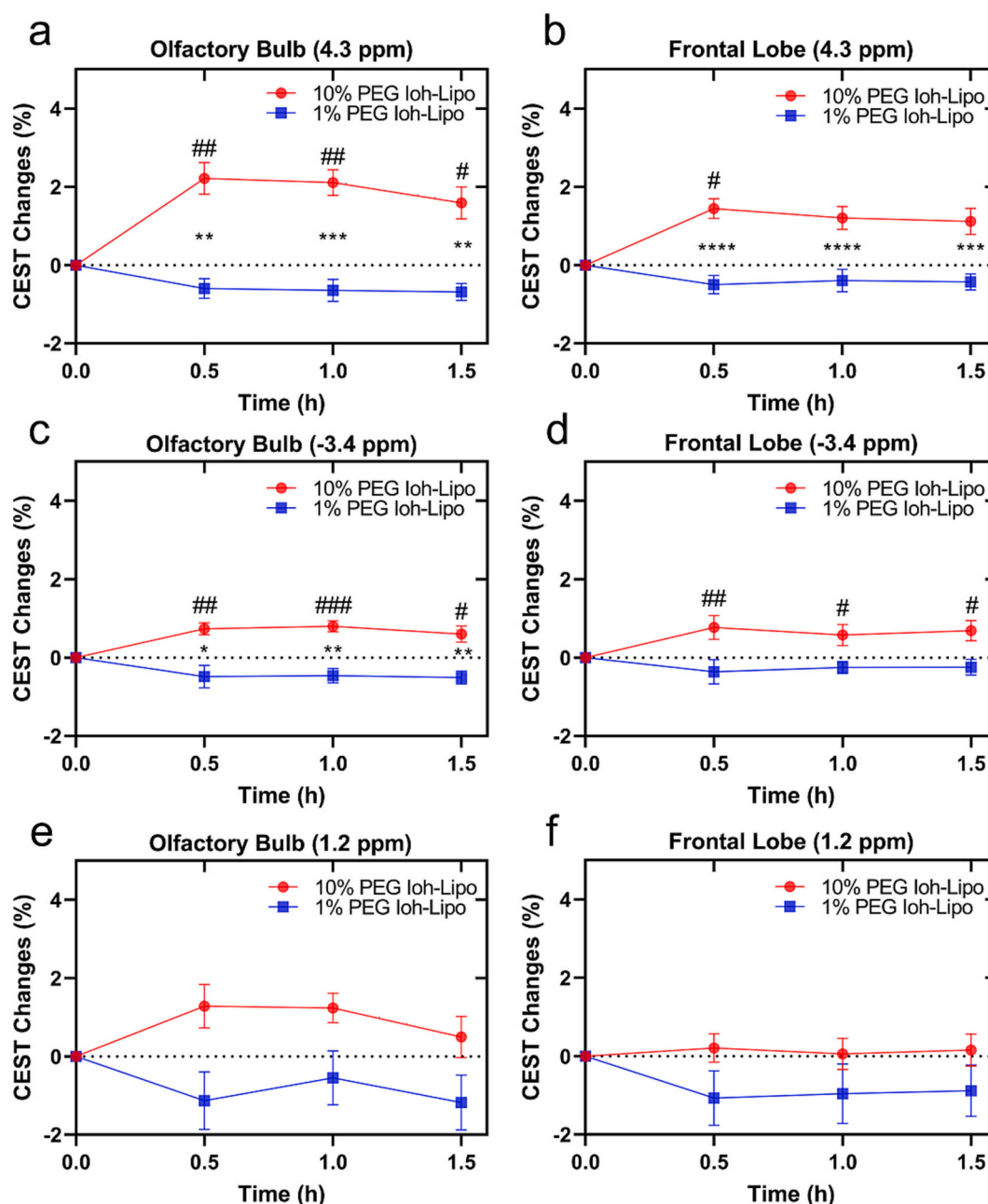
Fig. 6. CEST signal changes after intranasal administration of different PEG concentration Ioh-Lipo in frontal lobe and olfactory bulb (n = 6). CEST signal changes in OB (a) at 4.3 ppm, (c) -3.4 ppm and (e) 1.2 ppm. CEST signal changes in FL (b) at 4.3 ppm, (d) at −3.4 ppm and (f) at 1.2 ppm. Comparisons were made for different groups (*) and different time points (#) using 2-way ANOVA multiple comparison. Differences were considered as statistically significant for *P* value <0.05 (*/#), *P* < 0.01 (**/##), *P* < 0.001 (***/###), and *P* < 0.0001 (****/####).

received 10% PEG and 1% PEG Ioh-Lipo injections. Mice received 10% PEG Ioh-Lipo showed obviously higher distribution of rhodamine-labeled liposomes in both FL and OB compared to the mice received 1% PEG Ioh-Lipo (Fig. 8a, b). Notably, strong rhodamine signal was observed in specific regions including EPL + LROB, GCL, OL and FL (Fig. 8a). These observations echo the MRI findings (Fig. 5-7), thus confirming the contributions of Ioh-Lipo to CEST contrasts after intranasal administration in vivo. We did not include the edges of olfactory bulb for comparisons due to autofluorescence.

4. Discussions

This study demonstrated that our current design of CT contrast agent (iohexol) loaded liposomes with >10% PEG enables the imaging of nose-to-brain delivery using multiple CEST contrast. Iohexol has amide protons, which generated strong CEST contrast at 4.3 ppm (Fig. 2). After being loaded into liposome (Ioh-Lipo), the CEST contrast at 4.3 ppm remained high (at 35%, B_1 = 0.6 μT). When compared with other CT contrast agents, such as iopamidol [43,49,79], iohexol is preferred in this application, which has a single CEST contrast for assessing the delivery of intraliposomal agents in the brain at 3T. This could avoid overlapping readouts when assessing multiple components of the delivery system in vivo. Moreover, additional CEST contrast of 1.8% at −3.4 ppm and 20.6% at 1.2 ppm were observed in Ioh-Lipo (Fig. 4), which can be used to indicate liposome distribution after administration. According to our previous findings [21,51], the CEST contrast at −3.4 ppm originated from liposomes. While the CEST contrast at around 1.2 ppm might be mainly contributed by hydroxyl protons PEG as it was
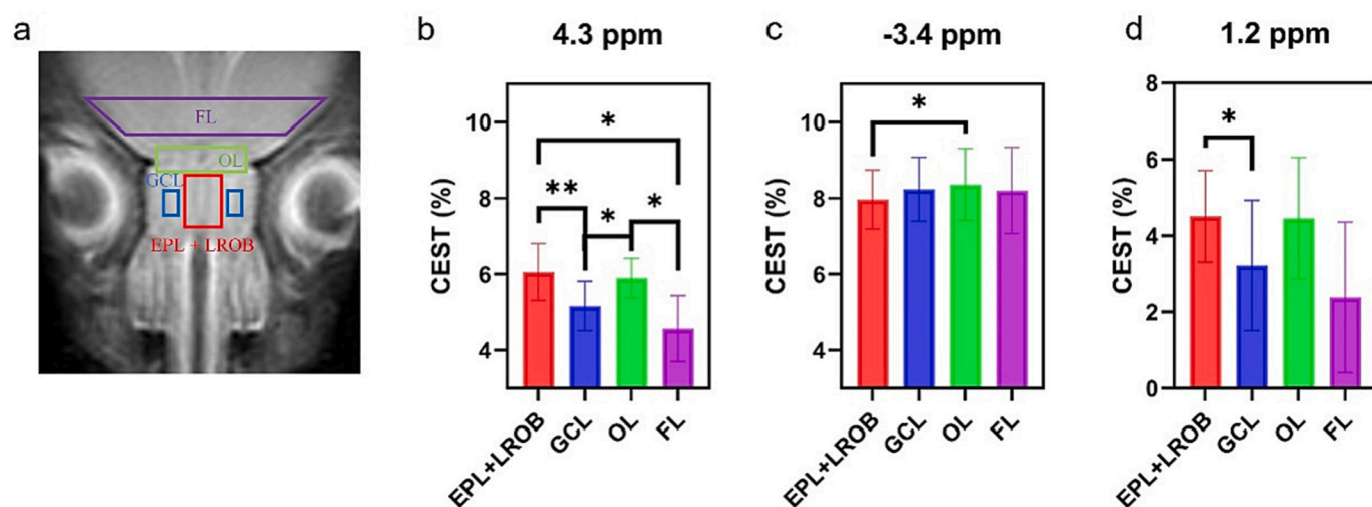
Fig. 7. ROI analysis in different regions in the olfactory bulb and the frontal lobe. (a) T2w image with ROIs drawn for 4 different regions. ROI analysis at (b) 4.3 ppm and (c) at −3.4 ppm. OB: olfactory bulb, FL (purple): frontal lobe, EPL + LROB (red): external plexiform layer + middle region between left and right OB, GCL (blue): granule cell layer, OL (green): olfactory limbus (OL) between OB and FL. Comparisons were made between the groups using one-way ANOVA. Differences were considered as statistically significant for P value <0.05 (*), $P < 0.01$ (**), and $P < 0.001$ (***). (For interpretation of the references to colour in this figure legend, the reader is referred to the web version of this article.)

higher in 10% PEG Ioh-Lipo than in 1% PEG Ioh-Lipo (Fig. 4b). Therefore, the Ioh-Lipo generated three distinctive CEST contrast at 4.3 ppm, −3.4 ppm and 1.2 ppm, which could be used to indicate the distributions of iohexol and liposome independently and simultaneously.

As the percentage of PEG in the liposome formulation is one of the determining factors to overcome the mucus barrier in the nasal cavity [12,13,80], we studied two liposome formulations, i.e. 10% PEG Ioh-Lipo and 1% PEG Ioh-Lipo. The 10% PEG Ioh-Lipo had a > 10 times higher PEG than 1% PEG Ioh-Lipo validated by NMR (Supplementary Fig. 1). The 10% PEG Ioh-Lipo had a significant 28.1% higher mucus retention compared to 1% PEG Ioh-Lipo in vitro ($P < 0.001$, Fig. 3b). Moreover, our results showed that liposomes with size >200 nm cannot reach the brain (Supplementary Fig. 8). Thus, Ioh-Lipo with >10% PEG and a comparable particle size to the mesh size of nasal mucus, the mesh size of nasal mucus is around 150 ± 50 nm [81], were able to pass the mucus and deliver drug to the brain.

CEST contrast at 4.3 ppm, −3.4 ppm and 1.2 ppm increased substantially in both OB and FL after intranasal administration of 10% PEG Ioh-Lipo in vivo (Fig. 5a). Moreover, characteristic peaks were observed at the corresponding frequencies (Fig. 5c,d). There was no such increase in case of 1% PEG Ioh-Lipo (Fig. 5b, e, f). With the reference to our in vitro cell retention study, mucus retention of 10% PEG Ioh-Lipo was significantly higher than 1% PEG Ioh-Lipo (Fig. 3). Moreover, the mucus penetration efficiency was reported to be significantly higher in high PEGylated liposomes than in low PEGylated liposomes [12–18,68]. Our in vivo intranasal MRI study shows a comparable result, this indicated that 10% PEG Ioh-Lipo shows a higher mucus retention properties than that of 1% PEG Ioh-Lipo. Hence, only 10% PEG Ioh-Lipo can be penetrated through the nasal mucus and be delivered to the OB and FL. Interestingly CEST at 4.3 ppm (Fig. 6a, b) is higher in OB than in FL, while CEST at −3.4 ppm (Fig. 6c, d) is comparable in OB and FL. At 0.5 h after injection, CEST contrast at 4.3 ppm increased by 62.0% ($p < 0.05$) in OB and by 39.5.2% ($p < 0.05$) in FL, while CEST contrast at −3.4 ppm increased by 10.9% ($p < 0.01$) in OB and by 9.2% in FL. There is no significant change at 1.2 ppm. With reference to our in vitro study, these two CEST contrast representing iohexol (at 4.3 ppm) and lipid bilayer (at −3.4 ppm) of the Ioh-Lipo. Since the intraliposomal iohexol could be released from Ioh-Lipo (Fig. 3a), the 10% PEG Ioh-Lipo release was about 36% in an hour. Therefore, we calculated the estimated dose of iohexol and liposome delivery from OB to FL based on the CEST contrast. We found that 57% of iohexol (4.3 ppm) was delivered from the OB to

FL, while 87% of liposome (−3.4 ppm) was delivered from the OB to the FL. The percentage difference of estimated dose is around 30% at 0.5 h which is comparable to the Ioh-Lipo release profile in vitro. This indicated there was a certain amount of iohexol could leak out from liposomes.

These observations prompted us to further study the sub-regional changes (Fig. 7). For mice received 10% PEG Ioh-Lipo, the CEST contrast at 4.3 ppm of FL was lower than that of regions in OB (EPL + LROB, GCL), as well as OL. High CEST contrast at 4.3 ppm was observed in outer regions, such as EPL + LROB and OL, which is CSF rich regions. The highest CEST contrast at 4.3 ppm was in the EPL + LROB. This could be coming from released iohexol and/or intraliposomal iohexol. There is no substantial difference of CEST contrast at −3.4 ppm and 1.2 ppm among all ROIs. This indicated that the liposome was evenly distributed in OB and FL. These also echoed that the CEST contrast at 4.3 ppm was much higher in OB than FL at 0.5 h after injection (Fig. 6), while CEST contrast at −3.4 ppm was more comparable between OB and FL during the monitored period.

We observed higher signal of rhodamine-labeled liposomes in mice received 10% PEG Ioh-Lipo compared to mice received 1% PEG Ioh-Lipo (Fig. 8). Moreover, this stronger signal was found in all sub-regions, i.e., EPL + LROB, GCL, OL, FL, which agreed with our CEST findings at −3.4 ppm and 1.2 ppm (Fig. 5,6) and in the histology (Fig. 8). Although we could not detect the iohexol in histology, the high and unique CEST contrast at 4.3 ppm in these regions of the brain indicated the successful delivery of Ioh-Lipo, especially in EPL + LROB and OL which are CSF rich regions. In vivo study showed that CEST contrast of 10% PEG Ioh-Lipo peaked at 0.5 h (4.3 ppm) and 1.0 h (−3.4 ppm) in the OB. Since lipophilic molecules are more likely to transport through intracellular olfactory pathway and trigeminal pathway, while solute and water are more likely to transport through transcellular pathway [78,82,83]. Furthermore, high mucus retention or penetration could lead to high brain uptake [78]. We observed the 10% PEG Ioh-Lipo transported into the OB and FL within 30 min [83], and the histological findings suggested that liposome distributions could be a result of successful delivery of lipophilic molecules into the brain through intracellular olfactory pathway [22,25,83–85]. Thus, imaging the amount of liposomes delivered from the nose to the brain and the distribution in brain regions that related to the delivery pathways could provide valuable information to develop the best formulation for drug delivery to the brain. This could also serve as an effective mean to guide the optimization of the
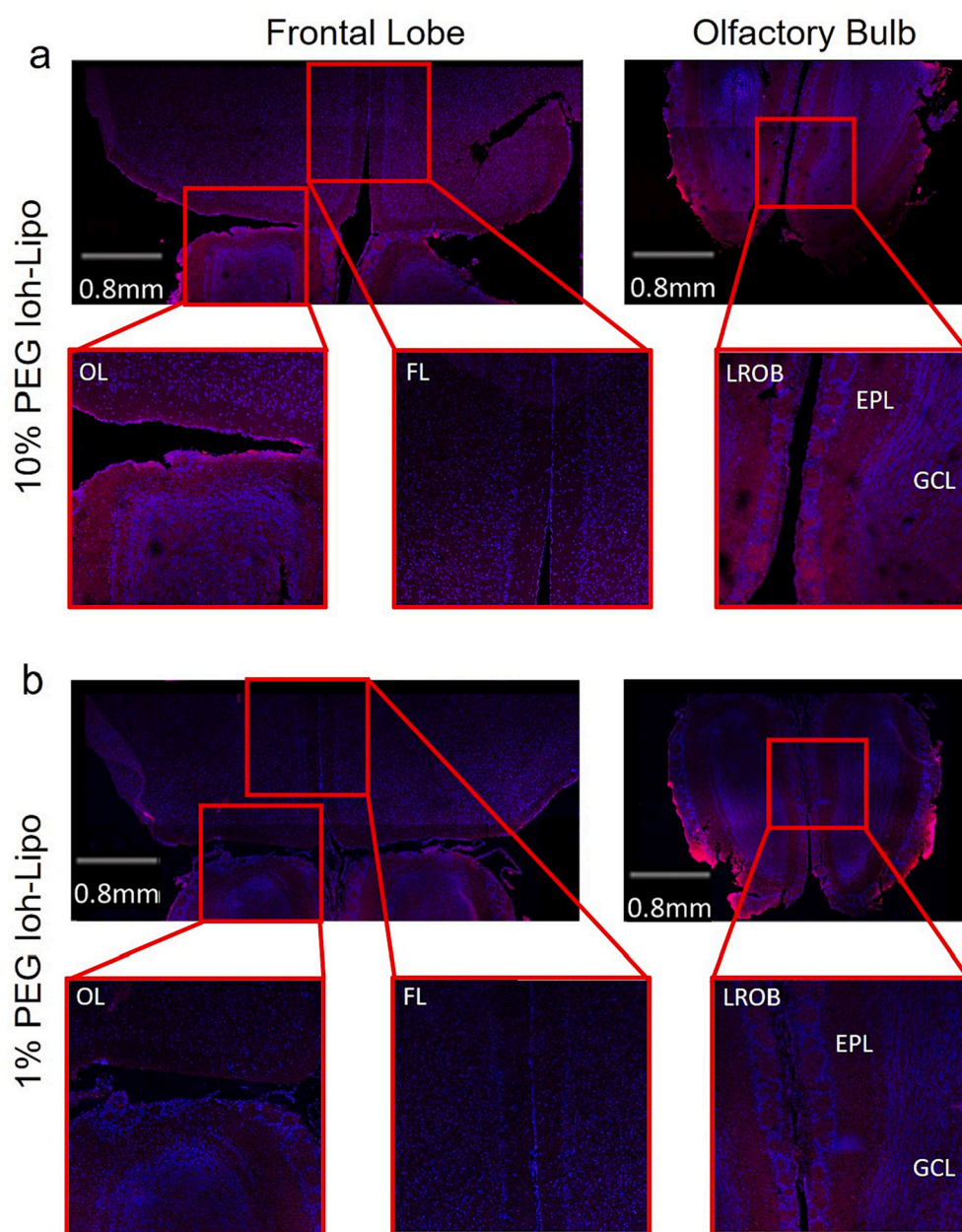
Fig. 8. Histological fluorescence images of mice received rhodamine-labeled liposomes with different PEG concentration. Rhodamine (red) indicated the distribution of rhodamine-labeled liposomes and DAPI (blue) was the counter stain for nuclei. Results of mice received (a) 10% PEG Ioh-Lipo and (b) 1% PEG Ioh-Lipo. OB: olfactory bulb, FL: frontal lobe, EPL + LROB: external plexiform layer + middle region between left and right OB, GCL: granule cell layer, OL: olfactory limbus (OL) between OB and FL. (For interpretation of the references to colour in this figure legend, the reader is referred to the web version of this article.)

formulation of delivery vehicles [22,23,67,78,82,83].

There are several limitations in our study. Although we observe a higher CEST contrast at 1.2 ppm for 10% PEG Ioh-Lipo than that of 1% PEG Ioh-Lipo in vivo, the longitudinal differences at this offset were not significant. This might be due to the large influence from DS effect since this offset is relatively close to the water signal at 0 ppm. It is quite challenging to extract accurate CEST contrast at 1.2 ppm of CEST data acquired at a 3T MRI scanner. Moreover, CEST MRI has a relatively lower spatial resolution than histology, the ROI analysis might not fully represent the regional observations under the microscope. For example, we can only draw the EPL + LROB as a single ROI for CEST contrast analysis of these two regions.

5. Conclusion

In conclusion, we designed CT agent-loaded liposomes, and demonstrated an image-guided nose-to-brain drug delivery using multiple CEST contrast. The mucus penetrating property of iohexol-loaded liposome with >10% PEG was considerably higher than low PEG liposomes, especially with liposomes <200 nm. After intranasal administration to mouse brain, substantial increases in CEST contrast at 4.3 ppm and −3.4 ppm was observed in both OB and FL for 10% PEG Ioh-Lipo, but not 1% PEG Ioh-Lipo, which was validated by histology. Interestingly, the spatial and temporal changes at 4.3 ppm and −3.4 ppm were distinctive, which could be ascribed to the release of iohexol from Ioh-Lipo. Thus, demonstrating the need to monitor these multiple component changes using the multiple CEST contrast. This unique CEST contrast property and mucus penetrating property of Ioh-Lipo could facilitate the drug delivery to the brain via bypassing BBB; and to monitor the drug and liposome regional distributions in the brain. This regional distribution that related the delivery pathways could provide valuable information for the design of effective delivery vehicles for nose-to-brain drug delivery. This multiple CEST contrast approach enables image-guided nose-to-brain drug delivery in a non-invasive manner.

Author contributions

L.H.L. and K.W.Y.C. designed and performed experiments, processed data, and wrote the paper; J.H. helped with experiment setup, wrote the data processing code, interpreted the data, and edited the paper; P.X. and X.H. helped with the liposome preparation and characterization. Y.L. helped with the data processing code. Z.C. and J.H.C.L. helped with the animals handling. G.W.Y.C and K—H.T helped with the cryosectioning and staining for histology.

Funding

CRediT authorship contribution statement

Lok Hin Law: Conceptualization, Methodology, Formal analysis, Investigation, Data curation, Writing – original draft, Writing – review & editing, Visualization. **Jianpan Huang:** Conceptualization, Methodology, Software, Data curation, Writing – review & editing, Visualization. **Peng Xiao:** Investigation. **Yang Liu:** Software. **Zilin Chen:** Investigation. **Joseph H.C. Lai:** Investigation. **Xiongqi Han:** Investigation. **Gerald W.Y. Cheng:** Investigation. **Kai-Hei Tse:** Investigation. **Kannie W.Y. Chan:** Conceptualization, Methodology, Writing – review & editing, Visualization, Supervision, Project administration, Funding acquisition.

Declaration of Competing Interest

The authors declare no competing interests.

Data availability

All the data that support the findings of this study are available within the article and its Supplementary Information. Source data are available from the corresponding author upon reasonable request.

Acknowledgements

Appendix A. Supplementary data

Supplementary data to this article can be found online at https://doi.org/10.1016/j.jconrel.2023.01.011.

References

[1] N.J. Abbott, A.A. Patabendige, D.E. Dolman, S.R. Yusof, D.J. Begley, Structure and function of the blood–brain barrier, Neurobiol. Dis. 37 (2010) 13–25.

[2] B. Sethi, V. Kumar, K. Mahato, D.W. Coulter, R.I. Mahato, Recent advances in drug delivery and targeting to the brain, J. Control. Release 350 (2022) 668–687.

[3] S. Wohlfart, S. Gelperina, J. Kreuter, Transport of drugs across the blood–brain barrier by nanoparticles, J. Control. Release 161 (2012) 264–273.

[4] A.R. Tekade, P.S. Mittha, C.S. Pisal, Nanostructured lipid carriers for nose to brain delivery targeting CNS: diversified role of liquid lipids for synergistic action, Advanced, Pharmac. Bull. 12 (2021) 763–771.

[5] J.P. Chovan, R.P. Klett, N. Rakieten, Comparison of meclizine levels in the plasma of rats and dogs after intranasal, intravenous, and oral administration, J. Pharm. Sci. 74 (1985) 1111–1113.

[6] W.A. Banks, J.E. Morley, M.L. Niehoff, C. Mattern, Delivery of testosterone to the brain by intranasal administration: comparison to intravenous testosterone, J. Drug Target. 17 (2009) 91–97.

[7] L.R. Hanson, A. Roeytenberg, P.M. Martinez, V.G. Coppes, D.C. Sweet, R.J. Rao, D. L. Marti, J.D. Hoekman, R.B. Matthews, W.H. Frey, Intranasal deferoxamine provides increased brain exposure and significant protection in rat ischemic stroke, J. Pharmacol. Exp. Ther. 330 (2009) 679–686.

[8] A. D'Souza, S. Nozohouri, B.S. Bleier, M.M. Amiji, CNS delivery of nucleic acid therapeutics: beyond the blood–brain barrier and towards specific cellular targeting, Pharm. Res. (2022) 1–29.

[9] C.D. Wurster, B. Winter, K. Wollinsky, A.C. Ludolph, Z. Uzelac, S. Witzel, M. Schocke, R. Schneider, T. Kocak, Intrathecal administration of nusinersen in adolescent and adult SMA type 2 and 3 patients, J. Neurol. 266 (2019) 183–194.

[10] S.S. Sadekar, M. Bowen, H. Cai, S. Jamalian, H. Rafidi, W. Shatz-Binder, J. Lafrance-Vanasse, P. Chan, W.J. Meilandt, A. Oldendorp, Translational approaches for brain delivery of biologics via cerebrospinal fluid, Clin. Pharmacol. Therap. 111 (2022) 826–834.

[11] L. Du, G. Zhao, Y. Lin, H. Sui, C. Chan, S. Ma, Y. He, S. Jiang, C. Wu, K.-Y. Yuen, Intranasal vaccination of recombinant adeno-associated virus encoding receptor-binding domain of severe acute respiratory syndrome coronavirus (SARS-CoV) spike protein induces strong mucosal immune responses and provides long-term protection against SARS-CoV infection, J. Immunol. 180 (2008) 948–956.

[12] T. Yu, K.W. Chan, A. Anonuevo, X. Song, B.S. Schuster, S. Chattopadhyay, Q. Xu, N. Oskolkov, H. Patel, L.M. Ensign, Liposome-based mucus-penetrating particles (MPP) for mucosal theranostics: demonstration of diamagnetic chemical exchange saturation transfer (diaCEST) magnetic resonance imaging (MRI), Nanomedicine 11 (2015) 401–405.

[13] J.S. Suk, Q. Xu, N. Kim, J. Hanes, L.M. Ensign, PEGylation as a strategy for improving nanoparticle-based drug and gene delivery, Adv. Drug Deliv. Rev. 99 (2016) 28–51.

[14] L.M. Ensign, B.C. Tang, Y.-Y. Wang, A.T. Terence, T. Hoen, R. Cone, J. Hanes, Mucus-penetrating nanoparticles for vaginal drug delivery protect against herpes simplex virus, Sci. Transl. Med. 4 (2012), 138ra179-138ra179.

[15] Q. Xu, L.M. Ensign, N.J. Boylan, A. Schon, X. Gong, J.C. Yang, N.W. Lamb, S. Cai, T. Yu, E. Freire, J. Hanes, Impact of surface polyethylene glycol (PEG) density on biodegradable nanoparticle transport in mucus ex vivo and distribution in vivo, ACS Nano 9 (2015) 9217–9227.

[16] Y.Y. Wang, S.K. Lai, J.S. Suk, A. Pace, R. Cone, J. Hanes, Addressing the PEG mucoadhesivity paradox to engineer nanoparticles that "slip" through the human mucus barrier, Angew. Chem. 47 (2008) 9726–9729.

[17] H.C. Zierden, A. Josyula, R.L. Shapiro, H.T. Hsueh, J. Hanes, L.M. Ensign, Avoiding a sticky situation: bypassing the mucus barrier for improved local drug delivery, Trends Mol. Med. 27 (2021) 436–450.

[18] S.K. Lai, Y.-Y. Wang, J. Hanes, Mucus-penetrating nanoparticles for drug and gene delivery to mucosal tissues, Adv. Drug Deliv. Rev. 61 (2009) 158–171.

[19] G.A. Duncan, J. Jung, J. Hanes, J.S. Suk, The mucus barrier to inhaled gene therapy, Mol. Ther. 24 (2016) 2043–2053.

[20] V.Y. Lin, N. Kaza, S.E. Birket, H. Kim, L.J. Edwards, J. LaFontaine, L. Liu, M. Mazur, S.A. Byzek, J. Hanes, Excess mucus viscosity and airway dehydration impact COPD airway clearance, Eur. Respir. J. 55 (2020).

[21] K.W. Chan, T. Yu, Y. Qiao, Q. Liu, M. Yang, H. Patel, G. Liu, K.W. Kinzler, B. Vogelstein, J.W. Bulte, A diaCEST MRI approach for monitoring liposomal accumulation in tumors, J. Control. Release 180 (2014) 51–59.

[22] L. Battaglia, P.P. Panciani, E. Muntoni, M.T. Capucchio, E. Biasibetti, P. De Bonis, S. Mioletti, M. Fontanella, S. Swaminathan, Lipid nanoparticles for intranasal administration: application to nose-to-brain delivery, Expert Opin. Drug Deliv. 15 (2018) 369–378.

[23] A.C. Correia, A.R. Monteiro, R. Silva, J.N. Moreira, J.M. Sousa Lobo, A.C. Silva, Lipid nanoparticles strategies to modify pharmacokinetics of central nervous system targeting drugs: crossing or circumventing the blood–brain barrier (BBB) to manage neurological disorders, Adv. Drug Deliv. Rev. 189 (2022), 114485.

[24] M. Yang, T. Yu, Y.Y. Wang, S.K. Lai, Q. Zeng, B. Miao, B.C. Tang, B.W. Simons, L. M. Ensign, G. Liu, Vaginal delivery of paclitaxel via nanoparticles with non-mucoadhesive surfaces suppresses cervical tumor growth, Adv. Healthc. Mater. 3 (2014) 1044–1052.

[25] M. Agrawal, S. Saraf, S. Saraf, S.G. Antimisiaris, M.B. Chougule, S.A. Shoyele, A. Alexander, Nose-to-brain drug delivery: an update on clinical challenges and progress towards approval of anti-Alzheimer drugs, J. Control. Release 281 (2018) 139–177.

[26] S. Bahadur, D.M. Pardhi, J. Rautio, J.M. Rosenholm, K. Pathak, Intranasal nanoemulsions for direct nose-to-brain delivery of actives for cns disorders, Pharmaceutics 12 (2020) 1230.

[27] P.C. Van Zijl, N.N. Yadav, Chemical exchange saturation transfer (CEST): what is in a name and what isn't? Magn. Reson. Med. 65 (2011) 927–948.

[28] K. Ward, A. Aletras, R.S. Balaban, A new class of contrast agents for MRI based on proton chemical exchange dependent saturation transfer (CEST), J. Magn. Reson. 143 (2000) 79–87.

[29] J. Zhou, J.-F. Payen, D.A. Wilson, R.J. Traystman, P.C. Van Zijl, Using the amide proton signals of intracellular proteins and peptides to detect pH effects in MRI, Nat. Med. 9 (2003) 1085–1090.

[30] J. Zhou, B. Lal, D.A. Wilson, J. Laterra, P.C. Van Zijl, Amide proton transfer (APT) contrast for imaging of brain tumors, Magn. Reson. Med. 50 (2003) 1120–1126.

[31] J. Huang, J.H. Lai, K.-H. Tse, G.W. Cheng, Y. Liu, Z. Chen, X. Han, L. Chen, J. Xu, K. W. Chan, Deep neural network based CEST and AREX processing: application in imaging a model of Alzheimer's disease at 3 T, Magn. Reson. Med. 87 (2022) 1529–1545.

[32] J. Huang, P.C. van Zijl, X. Han, C.M. Dong, G.W. Cheng, K.-H. Tse, L. Knutsson, L. Chen, J.H. Lai, E.X. Wu, Altered d-glucose in brain parenchyma and cerebrospinal fluid of early Alzheimer's disease detected by dynamic glucose-enhanced MRI, Sci. Adv. 6 (2020) eaba3884.

[33] K.W. Chan, M.T. McMahon, Y. Kato, G. Liu, J.W. Bulte, Z.M. Bhujwalla, D. Artemov, P.C. van Zijl, Natural D-glucose as a biodegradable MRI contrast agent for detecting cancer, Magn. Reson. Med. 68 (2012) 1764–1773.

[34] S. Walker-Samuel, R. Ramasawmy, F. Torrealdea, M. Rega, V. Rajkumar, S. P. Johnson, S. Richardson, M. Gonçalves, H.G. Parkes, E. Årstad, In vivo imaging of glucose uptake and metabolism in tumors, Nat. Med. 19 (2013) 1067–1072.

[35] K. Cai, A. Singh, H. Poptani, W. Li, S. Yang, Y. Lu, H. Hariharan, X.J. Zhou, R. Reddy, CEST signal at 2 ppm (CEST@ 2ppm) from Z-spectral fitting correlates with creatine distribution in brain tumor, NMR Biomed. 28 (2015) 1–8.

[36] K. Cai, M. Haris, A. Singh, F. Kogan, J.H. Greenberg, H. Hariharan, J.A. Detre, R. Reddy, Magnetic resonance imaging of glutamate, Nat. Med. 18 (2012) 302–306.

[37] F. Kogan, A. Singh, C. Debrosse, M. Haris, K. Cai, R.P. Nanga, M. Elliott, H. Hariharan, R. Reddy, Imaging of glutamate in the spinal cord using GluCEST, Neuroimage 77 (2013) 262–267.

[38] L. Chen, Z. Wei, K.W. Chan, Y. Li, K. Suchal, S. Bi, J. Huang, X. Xu, P.C. Wong, H. Lu, D-glucose uptake and clearance in the tauopathy Alzheimer's disease mouse brain detected by on-resonance variable delay multiple pulse MRI, J. Cereb. Blood Flow Metab. 41 (2021) 1013–1025.

[39] J. Huang, J.H. Lai, X. Han, Z. Chen, P. Xiao, Y. Liu, L. Chen, J. Xu, K.W. Chan, Sensitivity schemes for dynamic glucose-enhanced magnetic resonance imaging to detect glucose uptake and clearance in mouse brain at 3 T, NMR Biomed 35 (2022) e4640.

[40] C.K. Jones, M.J. Schlosser, P.C. Van Zijl, M.G. Pomper, X. Golay, J. Zhou, Amide proton transfer imaging of human brain tumors at 3T, Magn. Reson. Med. 56 (2006) 585–592.

[41] J. Zhou, J.O. Blakeley, J. Hua, M. Kim, J. Laterra, M.G. Pomper, P.C. Van Zijl, Practical data acquisition method for human brain tumor amide proton transfer (APT) imaging, Magn. Reson. Med. 60 (2008) 842–849.

[42] S. Goerke, Y. Soehngen, A. Deshmane, M. Zaiss, J. Breitling, P.S. Boyd, K. Herz, F. Zimmermann, K.D. Klika, H.P. Schlemmer, Relaxation-compensated APT and rNOE CEST-MRI of human brain tumors at 3 T, Magn. Reson. Med. 82 (2019) 622–632.

[43] S. Aime, L. Calabi, L. Biondi, M. De Miranda, S. Ghelli, L. Paleari, C. Rebaudengo, E. Terreno, Iopamidol: exploring the potential use of a well-established x-ray contrast agent for MRI, magnetic resonance in medicine: an official journal of the international society for, Magn. Reson. Med. 53 (2005) 830–834.

[44] P.Z. Sun, A.G. Sorensen, Imaging pH using the chemical exchange saturation transfer (CEST) MRI: correction of concomitant RF irradiation effects to quantify CEST MRI for chemical exchange rate and pH, Magn. Reson. Med. 60 (2008) 390–397.

[45] L.Q. Chen, C.M. Howison, J.J. Jeffery, I.F. Robey, P.H. Kuo, M.D. Pagel, Evaluations of extracellular pH within in vivo tumors using acidoCEST MRI, Magn. Reson. Med. 72 (2014) 1408–1417.

[46] B.F. Moon, K.M. Jones, L.Q. Chen, P. Liu, E.A. Randtke, C.M. Howison, M.D. Pagel, A comparison of iopromide and iopamidol, two acidoCEST MRI contrast media that measure tumor extracellular pH, Contrast Med. Mol. Imag. 10 (2015) 446–455.

[47] A. Anemone, L. Consolino, D.L. Longo, MRI-CEST assessment of tumour perfusion using X-ray iodinated agents: comparison with a conventional Gd-based agent, Eur. Radiol. 27 (2017) 2170–2179.

[48] E. Terreno, D.D. Castelli, S. Aime, Encoding the frequency dependence in MRI contrast media: the emerging class of CEST agents, Contrast Med. Mol. Imag. 5 (2010) 78–98.

[49] Z. Chen, Y. Li, R. Airan, Z. Han, J. Xu, K.W. Chan, Y. Xu, J.W. Bulte, P.C. Van Zijl, M.T. McMahon, CT and CEST MRI bimodal imaging of the intratumoral distribution of iodinated liposomes, Quant. Imag. Med. Surg. 9 (2019) 1579.

[50] G. Liu, M. Moake, Y.E. Har-El, C.M. Long, K.W. Chan, A. Cardona, M. Jamil, P. Walczak, A.A. Gilad, G. Sgouros, In vivo multicolor molecular MR imaging using diamagnetic chemical exchange saturation transfer liposomes, Magn. Reson. Med. 67 (2012) 1106–1113.

[51] X. Han, J. Huang, A.K. To, J.H. Lai, P. Xiao, X. Wu, J. Xu, K.W. Chan, CEST MRI detectable liposomal hydrogels for multiparametric monitoring in the brain at 3T, Theranostics 10 (2020) 2215.

[52] X. Han, J.H.C. Lai, J. Huang, S.W. Park, Y. Liu, K.W.Y. Chan, Imaging self-healing hydrogels and chemotherapeutics using CEST MRI at 3 T, ACS Appl. Bio Mater. 4 (2021) 5605–5616.

[53] C.K. Jones, A. Huang, J. Xu, R.A. Edden, M. Schär, J. Hua, N. Oskolkov, D. Zacà, J. Zhou, M.T. McMahon, Nuclear Overhauser enhancement (NOE) imaging in the human brain at 7 T, Neuroimage 77 (2013) 114–124.

[54] J. Xu, N.N. Yadav, A. Bar-Shir, C.K. Jones, K.W. Chan, J. Zhang, P. Walczak, M. T. McMahon, P.C. Van Zijl, Variable delay multi-pulse train for fast chemical exchange saturation transfer and relayed-nuclear overhauser enhancement MRI, Magn. Reson. Med. 71 (2014) 1798–1812.

[55] X.Y. Zhang, F. Wang, A. Afzal, J. Xu, J.C. Gore, D.F. Gochberg, Z. Zu, A new NOE-mediated MT signal at around −1.6ppm for detecting ischemic stroke in rat brain, Magn. Reson. Imaging 34 (2016) 1100–1106.

[56] J. Huang, X. Han, L. Chen, X. Xu, J. Xu, K.W. Chan, Relayed nuclear Overhauser enhancement imaging with magnetization transfer contrast suppression at 3 T, Magn. Reson. Med. 85 (2021) 254–267.

[57] J. Huang, J. Xu, J.H. Lai, Z. Chen, C.Y. Lee, H.K. Mak, K.H. Chan, K.W. Chan, Relayed nuclear Overhauser effect weighted (rNOEw) imaging identifies multiple sclerosis, NeuroImage: Clin. 32 (2021) 102867.

[58] J. Zhou, M. Zaiss, L. Knutsson, P.Z. Sun, S.S. Ahn, S. Aime, P. Bachert, J. O. Blakeley, K. Cai, M.A. Chappell, M. Chen, D.F. Gochberg, S. Goerke, H.Y. Heo, S. Jiang, T. Jin, S.G. Kim, J. Laterra, D. Paech, M.D. Pagel, J.E. Park, R. Reddy, A. Sakata, S. Sartoretti-Schefer, A.D. Sherry, S.A. Smith, G.J. Stanisz, P. C. Sundgren, O. Togao, M. Vandsburger, Z. Wen, Y. Wu, Y. Zhang, W. Zhu, Z. Zu, P. C.M. van Zijl, Review and consensus recommendations on clinical APT-weighted imaging approaches at 3T: application to brain tumors, Magn. Reson. Med. 88 (2022) 546–574.

[59] Y.C. Barenholz, Doxil®—the first FDA-approved nano-drug: lessons learned, J. Control. Release 160 (2012) 117–134.

[60] M.L. Briuglia, C. Rotella, A. McFarlane, D.A. Lamprou, Influence of cholesterol on liposome stability and on in vitro drug release, Drug Deliv. Transl. Res. 5 (2015) 231–242.

[61] M. Ramezanpour, D.P. Tieleman, Computational insights into the role of cholesterol in inverted hexagonal phase stabilization and endosomal drug release, Langmuir 38 (2022) 7462–7471.

[62] J.M. Zhao, Y.E. Har-el, M.T. McMahon, J. Zhou, A.D. Sherry, G. Sgouros, J. W. Bulte, P.C. van Zijl, Size-induced enhancement of chemical exchange saturation transfer (CEST) contrast in liposomes, J. Am. Chem. Soc. 130 (2008) 5178–5184.

[63] Z. Wang, N. Wang, S.-C. Cheng, K. Xu, Z. Deng, S. Chen, Z. Xu, K. Xie, M.-K. Tse, P. Shi, Phorbiplatin, a highly potent Pt (IV) antitumor prodrug that can be controllably activated by red light, Chem 5 (2019) 3151–3165.

[64] W.J. Duncanson, M.A. Figa, K. Hallock, S. Zalipsky, J.A. Hamilton, J.Y. Wong, Targeted binding of PLA microparticles with lipid-PEG-tethered ligands, Biomaterials 28 (2007) 4991–4999.

[65] H. Hatakeyama, H. Akita, K. Kogure, M. Oishi, Y. Nagasaki, Y. Kihira, M. Ueno, H. Kobayashi, H. Kikuchi, H. Harashima, Development of a novel systemic gene delivery system for cancer therapy with a tumor-specific cleavable PEG-lipid, Gene Ther. 14 (2007) 68–77.

[66] B.S. Schuster, J.S. Suk, G.F. Woodworth, J. Hanes, Nanoparticle diffusion in respiratory mucus from humans without lung disease, Biomaterials 34 (2013) 3439–3446.

[67] S. Ganger, K. Schindowski, Tailoring formulations for intranasal nose-to-brain delivery: a review on architecture, Physico-chemical characteristics and Mucociliary clearance of the nasal olfactory mucosa, Pharmaceutics 10 (2018).

[68] E.R. de Oliveira Junior, L.C.R. Santos, M.A. Salomao, T.L. Nascimento, G. de Almeida Ribeiro, L.M. Oliveira, E.M. Lima Liao, Nose-to-brain drug delivery mediated by polymeric nanoparticles: influence of PEG surface coating, Drug Deliv. Transl. Res. 10 (2020) 1688–1699.

[69] L.R. Hanson, J.M. Fine, A.L. Svitak, K.A. Faltesek, Intranasal administration of CNS therapeutics to awake mice, J. Vis. Exp. 74 (2013) e4440.

[70] M. Zaiss, P. Bachert, Chemical exchange saturation transfer (CEST) and MR Z-spectroscopy in vivo: a review of theoretical approaches and methods, Phys. Med. Biol. 58 (2013) R221.

[71] C.K. Jones, D. Polders, J. Hua, H. Zhu, H.J. Hoogduin, J. Zhou, P. Luijten, P.C. Van Zijl, In vivo three-dimensional whole-brain pulsed steady-state chemical exchange saturation transfer at 7 T, Magn. Reson. Med. 67 (2012) 1579–1589.

[72] M. Zaiß, B. Schmitt, P. Bachert, Quantitative separation of CEST effect from magnetization transfer and spillover effects by Lorentzian-line-fit analysis of z-spectra, J. Magn. Reson. 211 (2011) 149–155.

[73] X.Y. Zhang, F. Wang, H. Li, J. Xu, D.F. Gochberg, J.C. Gore, Z. Zu, Accuracy in the quantification of chemical exchange saturation transfer (CEST) and relayed nuclear Overhauser enhancement (rNOE) saturation transfer effects, NMR Biomed. 30 (2017), e3716.

[74] J. Huang, Z. Chen, S.-W. Park, J.H. Lai, K.W. Chan, Molecular imaging of brain tumors and drug delivery using CEST MRI: promises and challenges, Pharmaceutics 14 (2022) 451.

[75] M. Pozzoli, F. Sonvico, H.X. Ong, D. Traini, M. Bebawy, P. Young, Optimization of RPMI 2650 cells as a model for nasal mucosa, Respirat. Drug Deliv. 2014 (2014).

[76] V.S. Gonçalves, A.A. Matias, J. Poejo, A.T. Serra, C.M. Duarte, Application of RPMI 2650 as a cell model to evaluate solid formulations for intranasal delivery of drugs, Int. J. Pharm. 515 (2016) 1–10.

[77] M.E. Kreft, U.D. Jerman, E. Lasič, T.L. Rižner, N. Hevir-Kene, L. Peternel, K. Kristan, The characterization of the human nasal epithelial cell line RPMI 2650 under different culture conditions and their optimization for an appropriate in vitro nasal model, Pharm. Res. 32 (2015) 665–679.

[78] S.S. Hong, K.T. Oh, H.G. Choi, S.J. Lim, Liposomal formulations for nose-to-brain delivery: recent advances and future perspectives, Pharmaceutics 11 (2019).

[79] P. Xiao, J. Huang, X. Han, J.W. Cheu, Y. Liu, L.H. Law, J.H.C. Lai, J. Li, S.W. Park, C.C.L. Wong, R.H.W. Lam, K.W.Y. Chan, Monitor tumor pHe and response longitudinally during treatment using CEST MRI-detectable alginate microbeads, ACS Appl. Mater. Interfaces 14 (2022) 54401–54410.

[80] G. Osman, J. Rodriguez, S.Y. Chan, J. Chisholm, G. Duncan, N. Kim, A.L. Tatler, K. M. Shakesheff, J. Hanes, J.S. Suk, PEGylated enhanced cell penetrating peptide nanoparticles for lung gene therapy, J. Control. Release 285 (2018) 35–45.

[81] S.K. Lai, J.S. Suk, A. Pace, Y.-Y. Wang, M. Yang, O. Mert, J. Chen, J. Kim, J. Hanes, Drug carrier nanoparticles that penetrate human chronic rhinosinusitis mucus, Biomaterials 32 (2011) 6285–6290.

[82] T.T. Nguyen, T.T.D. Nguyen, N.M. Tran, G. Van Vo, Lipid-based Nanocarriers via nose-to-brain pathway for central nervous system disorders, Neurochem. Res. 47 (2022) 552–573.

[83] T.P. Crowe, M.H.W. Greenlee, A.G. Kanthasamy, W.H. Hsu, Mechanism of intranasal drug delivery directly to the brain, Life Sci. 195 (2018) 44–52.

[84] J.J. Lochhead, T.P. Davis, Perivascular and perineural pathways involved in brain delivery and distribution of drugs after intranasal administration, Pharmaceutics 11 (2019) 598.

[85] J.J. Lochhead, R.G. Thorne, Intranasal delivery of biologics to the central nervous system, Adv. Drug Deliv. Rev. 64 (2012) 614–628.